Remote Sensing of Environment 323 (2025) 114737

Contents lists available at ScienceDirect

Remote Sensing of Environment

journal homepage: www.elsevier.com/locate/rse

Towards resolution enhancement of P-band brightness temperature data using passive-passive downscaling with L-band radiometer data

Luisa F. White-Murillo [a,*], Jeffrey P. Walker [a], Nan Ye [a], James Hills [b], Xiaoling Wu [a], Lixiaozhou Zhou [a], Ziwei Xiong [a], Liujun Zhu [a], Brian Ng [c], Mahta Moghaddam [d], Simon Yueh [e]

[a] *Department of Civil and Environmental Engineering, Monash University, Clayton, Australia*
[b] *Tasmanian Institute of Agriculture, The University of Tasmania, Hobart, Australia*
[c] *School of Electrical and Mechanical Engineering, The University of Adelaide, Adelaide, Australia*
[d] *School of Engineering, University of Southern California, Los Angeles, USA*
[e] *Jet Propulsion Laboratory, California Institute of Technology, Pasadena, USA*

A R T I C L E I N F O

Edited by Jing M. Chen

Keywords:
P-band
L-band
Radiometer
Passive microwave
Spatial resolution
Downscaling

A B S T R A C T

Current space-borne L-band radiometers have been routinely providing global soil moisture maps every 2 to 3 days for more than 15 years. However, they can only estimate soil moisture in the top 5 cm of the soil, which limits its usefulness in applications that need deep layer soil moisture. Fortuitously, recent work has shown that there is a potential to retrieve root zone soil moisture (RZSM) when combining P-band radiometer data with L-band radiometer data at the same spatial resolution. Nevertheless, there are antenna size limitations that currently restrict L-band radiometer data to a resolution of 40 km. Accordingly, if the same antenna is used for a joint P-band (750 MHz) and L-band (1.4GHz) satellite mission, the footprint size at P-band will be double that attained at L-band, limiting its usefulness in applications and making joint interpretation difficult. It is therefore essential to downscale the P-band radiometer measurements to at least the same resolution as the L-band measurements. Consequently, this paper has explored three alternative passive-passive P-band downscaling algorithms using the spatial information that exists in the L-band radiometer data, to achieve P-band brightness temperature (Tb) information at the same resolution as the L-band passive measurements. Analysis was conducted using data from three airborne campaigns in south-eastern Australia, with resolutions ranging from 36 km to 200 m under a range of moisture conditions and spatial characteristics. The three alternate downscaling algorithms used in this paper, designated as Algorithm A, B, and C, were not only compared to determine which generated the best performance, but were also analysed according to different land cover types and seasons. The results demonstrated that the Smoothing Filter-based Intensity Modulation (SFIM) method, referred to as Algorithm A, outperformed the others, with a median root mean square error (RMSE) compared to the original observations of 3 K when downscaling to half of the original spatial resolution, increasing to around 8 K when downscaling to 36 times finer than the original resolution.

1. Introduction

Soil moisture is acknowledged as an essential climate variable due to its direct impact on land-atmosphere interactions, influencing the physical processes in climate change, climate variability, and vegetation conditions (Seneviratne et al., 2010; World Meteorological Organization, 2022). Moreover, with the world's population predicted to reach 10 billion by 2050, agricultural productivity will need to increase by 70 % to maintain food security (World Bank Group, 2021). Consequently, soil moisture information will play a critical role in ensuring that sustainable irrigation practices are applied in agriculture for achieving crop yield improvement and for more efficient water resources management (Merlin et al., 2013; Peng et al., 2021). Furthermore, it is the root zone soil moisture that is most important in governing the soil and plant dynamics for crop health, yield, and soil water monitoring, with around 75 % of plant roots being within the top 40 cm layer of soil globally (Jackson et al., 1996; Li et al., 2006).

Microwave radiometer observations at L-band have demonstrated a

---

* Corresponding author.
E-mail address: luisa.whitemurillo@monash.edu (L.F. White-Murillo).

https://doi.org/10.1016/j.rse.2025.114737
Received 30 October 2024; Received in revised form 12 March 2025; Accepted 31 March 2025

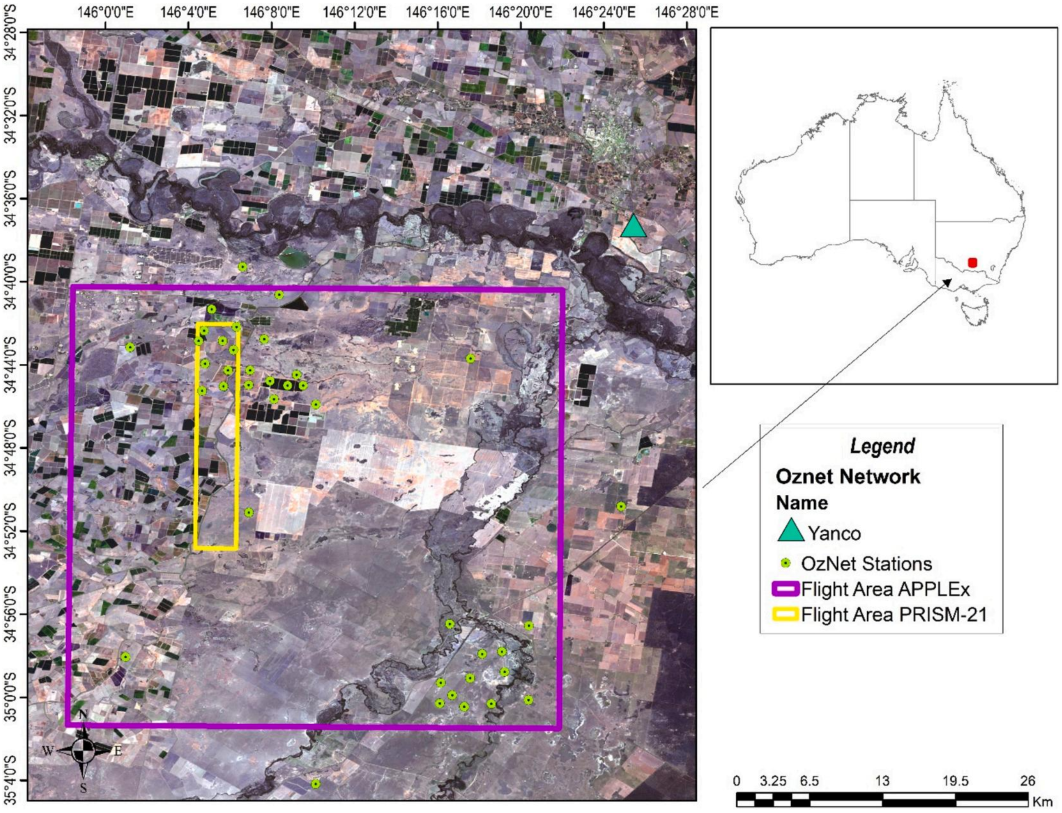

Fig. 1. The APPLEx-1/−2 and PRISM-21 campaign locations near Yanco NSW, Australia together with the OzNet soil moisture monitoring network station locations. A true colour Landsat-8 satellite image taken on 6 March 2021 is used as the background.

direct relationship with the dielectric properties of soil and water (Escorihuela et al., 2010; Wagner et al., 2007) for more than three decades (Engman and Chauhan, 1995), providing a capability to retrieve soil moisture information globally (Wigneron et al., 2017). While the success of L-band radiometer data for determining soil moisture has been demonstrated through satellite missions like Soil Moisture Active Passive (SMAP; Entekhabi et al., 2010) and Soil Moisture and Ocean Salinity (SMOS; Kerr et al., 2010), their soil moisture estimate is limited to the top 5 cm of the soil surface (Calvet et al., 2011) for areas with a canopy layer having not more than 5 kg/m^2 of Vegetation Water Content (VWC; O'Neill et al., 2021). Importantly, the capability for P-band observations to retrieve the soil moisture content over deeper soil layer depths (Shen et al., 2022; Ye et al., 2021) and for canopies with higher VWC (Shen et al., 2023) has been demonstrated. Consequently, P-band Tb at 750 MHz can be used to retrieve soil moisture to a depth of 10 cm or greater under drying conditions (Shen et al., 2021), and down to a depth of 28 cm depth or more with less than 0.04 m^3/m^3 *RMSE* when combined with observations of L-band Tb at 1.4GHz (Brakhasi et al., 2024b, 2024a, 2023). However, as the spatial resolution is proportional to the ratio of the wavelength and antenna size (Le Vine et al., 1989), a bigger antenna is required at P-band to maintain the 35 km to 50 km resolution of current L-band missions, having an antenna diameter of 6 m in SMAP (Entekhabi et al., 2014b), and an interferometric aperture synthesis antenna with an arm length of around 4.5 m in SMOS, resulting in an overall effective antenna size of around 8 m (Waldteufel et al., 2003). At 750 MHz, this would mean an antenna size of at least 12 m, being impractical for current satellite platforms. Importantly, this issue is not unique to observations at P-band. For example, the Copernicus Imaging Microwave Radiometer (CIMR) mission currently under development will have L-, C-, X-, K- and Ka-band radiometer channels with separate antenna feeds illuminating a deployable mesh reflector, being conically scanned on one satellite (Vanin et al., 2020). Consequently, it is planned to use the C-band data to downscale the L-band data from the same antenna (Zhang et al., 2023). Moreover, another mission under development, called CryoRad, will include a single feed radiometer operating in the range of 400 MHz – 2GHz, with an antenna formed by an offset reflector with a diameter of 6-8 m (Macelloni et al., 2018), providing different resolutions at each frequency, being 40 km and 8 km at P- and L-band respectively. Accordingly, a downscaling methodology will be needed to maintain the same spatial resolution for the L- and P-band observation frequencies to take advantage of using L- and P-band observations together for root zone soil moisture retrieval.

While previous downscaling methods have been tested to improve the resolution of L-band radiometer data (Sabaghy et al., 2020, 2017) by combining with higher frequency microwave radiometer observations such as X-, S-, and Ka-band (Lu et al., 2022; Yao et al., 2019; Ye et al., 2019), such an approach has not been tested at P-band. Moreover, those applications have been impacted by atmospheric effects, the influence of vegetation, and soil properties as roughness at the higher frequencies. Since L-band and P-band are less susceptible to atmospheric conditions compared to higher frequencies, and are less affected by vegetation and surface roughness, it is expected that good results can be achieved using a passive-passive downscaling approach, with the L-band observations used to downscale the P-band observations. However, it is noted that L-band has a different depth sensitivity to P-band, which can potentially impact the downscaling accuracy. Henceforth, this study has tested three linear downscaling relationships to increase the P-band resolution using L-band, and assessed their performance under different land cover types and seasonal conditions.

2. Data

The data used in this paper was collected during three campaigns; P-band Radiometer Inferred Soil Moisture-21 (PRISM-21), and Active-Passive P- and L-band Experiment-1 and -2 (APPLEx-1, APPLEx-2), located near Yanco NSW, Australia (Fig. 1). These campaigns were

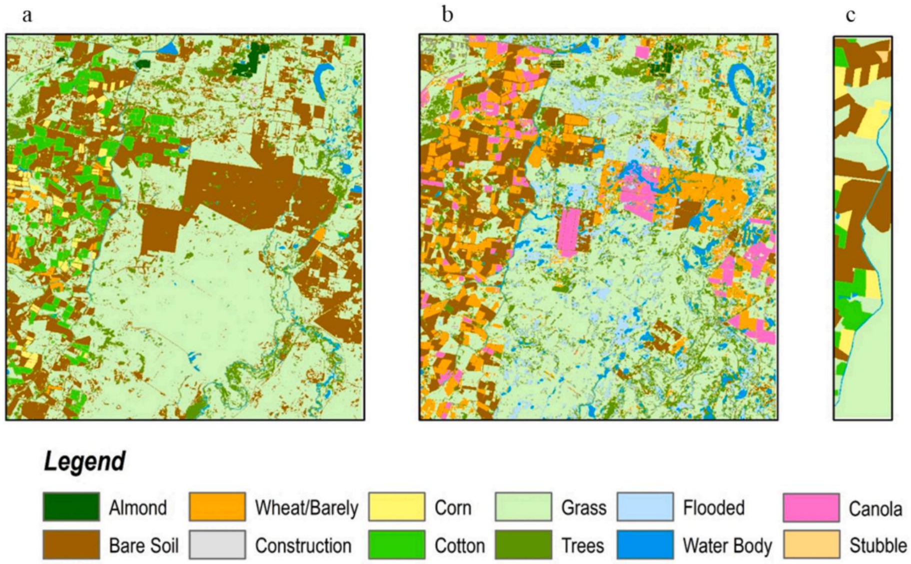

Fig. 2. Derived land cover maps for (a) APPLEx-1, (b) APPLEx-2, and (c) PRISM-21. Note the substantial increase in open water for APPLEx-2 due to localised flooding.

Table 1
Number of pixels that covered each land cover type for each campaign.

Land Cover Type	PRISM-21	APPLEx-1	APPLEx-2
Almond	–	5	3
Bare Soil	478	386	39
Wheat/Barely	–	11	43
Corn	164	15	–
Cotton	144	66	–
Grass	678	694	141
Trees	–	90	44
Canola	–	–	16
Stubble	7	–	–

conducted in March 2021, February 2022 and October 2022 respectively. APPLEx-1 data was acquired at 1 km resolution over an area of 36 km × 36 km to simulate a satellite pixel acquisition. Similarly, APPLEx-2 L-band data was acquired at 1 km while P-band data was at 2 km resolution across the same 36 km × 36 km area. In contrast, PRISM-21 was collected at 200 m resolution over a sub area of 3 km × 20 km.

The experimental aircraft was equipped with two passive microwave radiometers, installed in succession. The first was the Polarimetric L-band Multibeam Radiometer (PLMR) operating at 1.413GHz, dual-polarization, and six incidence angles ($\pm 7^\circ$, $\pm 21.5^\circ$ & $\pm 38.5^\circ$). The second was the Polarimetric P-band Multibeam Radiometer (PPMR) operating at 750 MHz, dual-polarization, and four incidence angles ($\pm 15^\circ$ & $\pm 45^\circ$). During the APPLEx campaigns, the instruments were installed in a pushbroom configuration, with the PLMR data angle normalized to 38.5° and PPMR data angle normalized to 45°, being their outer beams using a cumulative distribution function approach (Ye et al., 2015). As the flight design of PRISM-21 allowed full area coverage with the outer beams, angular normalization was not required. The PLMR and PPMR calibration was conducted using the Tb measurements from a calibration box at ambient temperature and the sky before and after each flight, and over a water body during flights for each of the airborne campaigns. The accuracy for PLMR was found to be 1.55 K ± 0.70 K at H polarization and 1.36 K ± 0.62 K at V polarization, while the PPMR calibration resulted in an accuracy of 2.82 K ± 1.04 K, and 3.34 K ± 1.56 K for H and V polarizations respectively.

Complementary ground data included in-situ stations from the OzNet network, recording precipitation, soil moisture and soil temperature every 20 min at 0–5 cm, 5–10 cm, 10–15 cm, 15–20 cm, 20–25 cm and 35–40 cm depth. This data allowed any brightness temperature bias introduced due to a timing mismatch to be assessed, as the PPMR and PLMR data were taken either on adjacent days (as in APPLEx-1) or a different time of the same day (as in PRISM-21 and APPLEx-2), since it was not possible to fly both PLMR and PPMR concurrently. To achieve this, the effective soil temperature (T_{eff}) of each station was calculated with the Wigneron et al. (2001) model. This analysis concluded that the expected error due to spatiotemporal changes in T_{eff} should typically be less than 4 K, and 6 K at most, the uncertainty of which could introduce an *RMSE* considerably less than 0.04 m^3/m^3 in soil moisture retrieval (Entekhabi et al., 2014b).

A regional driving route throughout the study area was followed to determine point-based land cover characteristics that were subsequently utilised to develop land cover maps for each campaign. These landcover maps were derived from a supervised classification with Bayes' theorem (Ahmad and Quegan, 2012) using Harmonized Sentinel and Landsat images (see Fig. 2). The resultant maps were aggregated to the same resolution as the collected Tb in each campaign with a pixel coverage as described in Table 1. Additional detailed information related to the PRISM and APPLEx campaigns can be found in the websites https://www.prism.monash.edu and https://www.applex.monash.edu respectively.

3. Methods

To provide an assessment across a wide range of spatial resolutions, including those used by SMAP and SMOS (Entekhabi et al., 2014b; Kerr et al., 2001), the radiometer data was aggregated in a mathematical sequence: the PRISM-21 Tb data was aggregated from the original 200 m to 3 km, 1 km, and 600 m to simulate coarser resolutions (Fig. 3), and subsequently, the aggregated coarser P-band Tb was disaggregated to 200 m resolution. Similarly, the APPLEx-1 Tb data was aggregated from 1 km resolution to 36 km, 18 km, 9 km, 3 km resolutions (Fig. 4) to simulate a satellite data acquisition of P-band Tb at 36 km resolution, and to evaluate disaggregation to 18 km, 9 km, 3 km, and 1 km resolutions. Moreover, the aggregated medium resolution of 18 km P-band Tb was disaggregated to 9 km, 3 km, and 1 km resolutions. Due to failure of one outer beam from PPMR during APPLEx-2, the flight height was adjusted to achieve full coverage of the study area within the allotted flight time. Accordingly, the APPLEx-2 P-band Tb observations had a spatial resolution of 2 km (rather than 1 km) and so was aggregated to

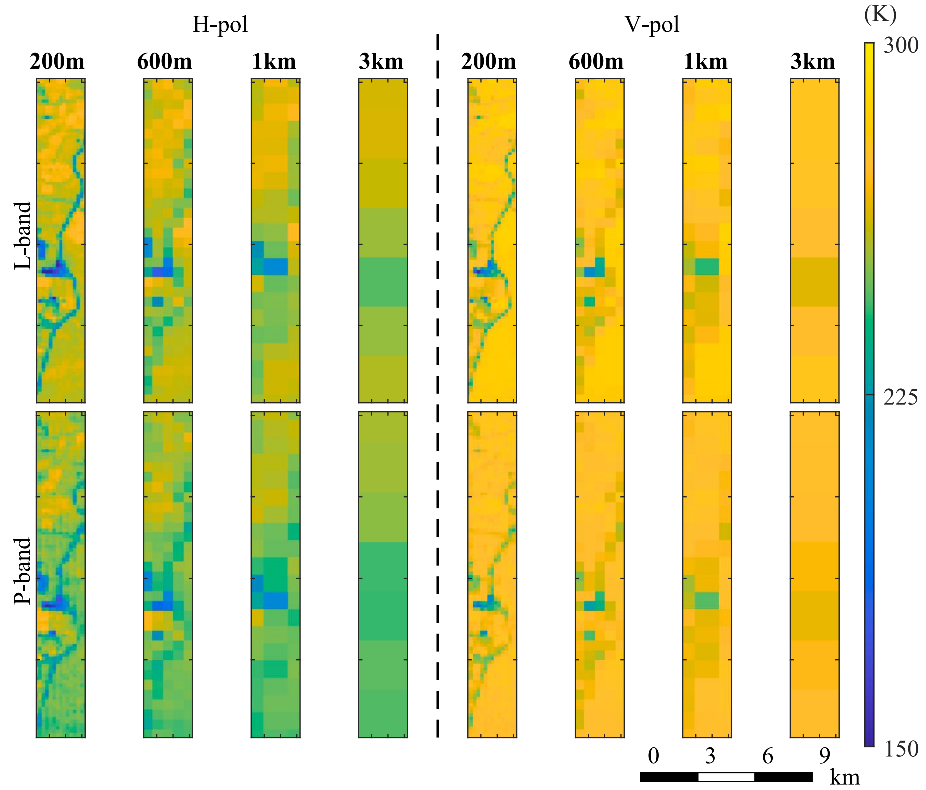

Fig. 3. An example of aggregated P- and L-band Tb in the bottom and top rows respectively, for PRISM-21 at H- (left) and V-polarization (right) on 9 March 2021, aggregated to the resolution shown at the top of the figure.

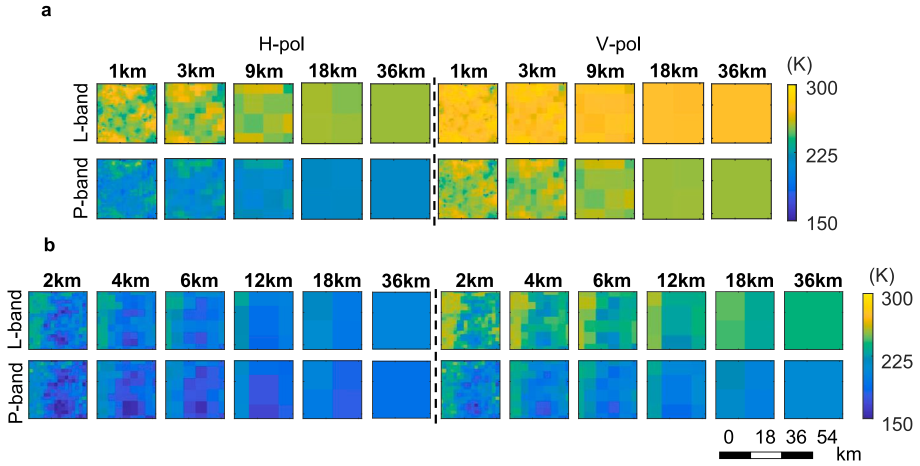

Fig. 4. As for Fig. 3 but for (a) APPLEx-1 on 1 February 2022 and (b) APPLEx-2 on 18 October 2022.

36 km, 18 km, 12 km, 6 km and 4 km resolutions (Fig. 4), with the 36 km P-band Tb resolution disaggregated to 18 km, 12 km, 6 km, 4 km, and 2 km resolutions. Moreover, the P-band Tb aggregated to a medium resolution of 18 km was disaggregated to 12 km, 6 km, 4 km, and 2 km resolutions. The aggregation method used the average cell approach previously used by Entekhabi et al. (2014b), whereby

$$\boldsymbol{Tb_p}(\boldsymbol{C}) = \frac{\boldsymbol{1}}{\boldsymbol{N}}\sum\nolimits_{\boldsymbol{N}=1}^{\boldsymbol{N}} \boldsymbol{Tb_p}(\boldsymbol{F}), \tag{1}$$

where N represents the number of pixels at the fine resolution in the coarse pixel, C refers to the brightness temperature at the coarse resolution, F refers to the brightness temperature at the fine resolution, and the subscript p refers to the polarization.

Three passive-passive multifrequency downscaling relationships, referred to as Algorithm A, B, and C in this paper, were tested for their ability to reliably downscale P-band Tb using L-band Tb, and their performance evaluated under different land cover types, moisture conditions and spatial resolutions. The Smoothing Filter-based Intensity Modulation (SFIM) downscaling method developed by Liu (2000), referred to as “Algorithm A" in this paper, is a multi-sensor combination that has been used to improve the L-band Tb resolution of SMAP using finer resolution Ka-band observations from the Advanced Microwave Scanning Radiometer 2 (AMSR2) (Ye et al., 2019). This approach has been evaluated with original 1.4 K accuracy aircraft L-band Tb data as a reference for the SMAPEx-4 and SMAPEx-5 campaigns (Sabaghy et al., 2020; Ye et al., 2019). Here, the L-band medium resolution was

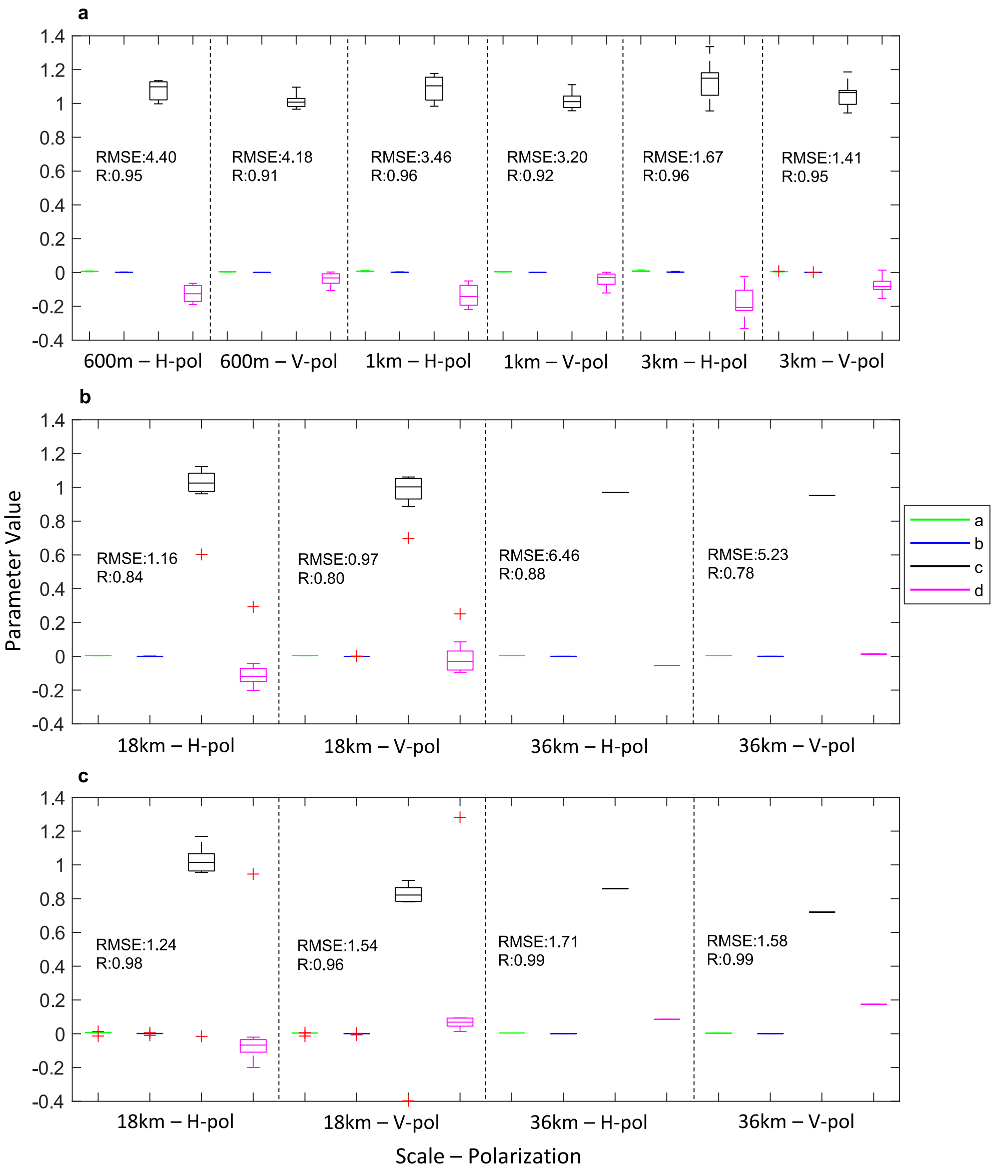

Fig. 5. Parameters used in Algorithm B for PRISM-21 (a), APPLEx-1 (b), and APPLEx-2 (c). The scale represents the coarse resolution from which the parameters were calibrated according to the corresponding polarization, In the case of 36 km the regression was per time so there is only one value in the box plot per each parameter. Meanwhile, the other scales represent the variability of the parameters throughout the campaigns. The average *RMSE* (K) and *R* represents the statistics metrics from the linear regression using the calibrated parameters.

aggregated to the same coarser resolution as P-band, with the downscaling factor using the coarse and medium resolution L-band data used to modulate the coarser resolution of P-band such that

$$\boldsymbol{TbP_p}(\boldsymbol{M}) = \frac{\boldsymbol{TbL_p}(\boldsymbol{M})}{\boldsymbol{TbL_p}(\boldsymbol{C})} {}^{*}\boldsymbol{TbP_p}(\boldsymbol{C}), \tag{2}$$

where *M* and *C* refers to the brightness temperature at medium and coarse resolution respectively, *TbP* is the brightness temperature at P-band, and *TbL* is the brightness temperature at L-band.

The brightness temperature disaggregation method “Algorithm B" proposed by Yao et al. (2019) was used to downscale aircraft-based L-band Tb using S-band Tb sampled at 800 m resolution. This method uses a linear relationship whereby slope and intercept are related to the microwave vegetation index (MVI; Shi et al., 2008; Shi and Li, 2013), in an effort to reduce vegetation effects. The equation includes four parameters (*a, b, c* and *d*) calculated from a spatial or temporal normal regression of the coarse resolution observations according to

$$\boldsymbol{\beta} = \left(\boldsymbol{X}^T\boldsymbol{X}\right)^{-1}\boldsymbol{X}^T\boldsymbol{y}, \tag{3}$$

$$\boldsymbol{TbP_p}(\boldsymbol{C}) = \boldsymbol{a}(\boldsymbol{C}) + \boldsymbol{c}(\boldsymbol{C})\frac{\boldsymbol{MVI}}{\overline{\boldsymbol{MVI}}} + \left(\boldsymbol{b}(\boldsymbol{C}) + \boldsymbol{d}(\boldsymbol{C})\frac{\boldsymbol{MVI}}{\overline{\boldsymbol{MVI}}}\right){}^{*}\boldsymbol{TbL_p}(\boldsymbol{C}), \tag{4}$$

$$\boldsymbol{MVI} = \frac{\boldsymbol{TbP_V}(\boldsymbol{C}) - \boldsymbol{TbP_H}(\boldsymbol{C})}{\boldsymbol{TbL_V}(\boldsymbol{C}) - \boldsymbol{TbL_H}(\boldsymbol{C})}, \tag{5}$$

where β is the matrix with the parameters *a*, *b*, *c*, and *d*; *X* is the matrix of the function inputs; and *y* is the matrix of the coarse P-band brightness temperature. $\overline{MVI}$is the mean (temporal or spatial) of the *MVI*, the subscript *V* refers to V polarization, and the subscript *H* refers to H polarization. The parameters are then applied to the downscaling algorithm to obtain a medium resolution P-band estimate using the medium resolution L-band observation according to

$$\boldsymbol{TbP_p}(\boldsymbol{M}) = \boldsymbol{a}(\boldsymbol{C}) + \boldsymbol{c}(\boldsymbol{C})\frac{\boldsymbol{MVI}}{\overline{\boldsymbol{MVI}}} + \left(\boldsymbol{b}(\boldsymbol{C}) + \boldsymbol{d}(\boldsymbol{C})\frac{\boldsymbol{MVI}}{\overline{\boldsymbol{MVI}}}\right){}^{*}\boldsymbol{Tb}\mathrm{L}_{\boldsymbol{p}}(\boldsymbol{M}). \tag{6}$$

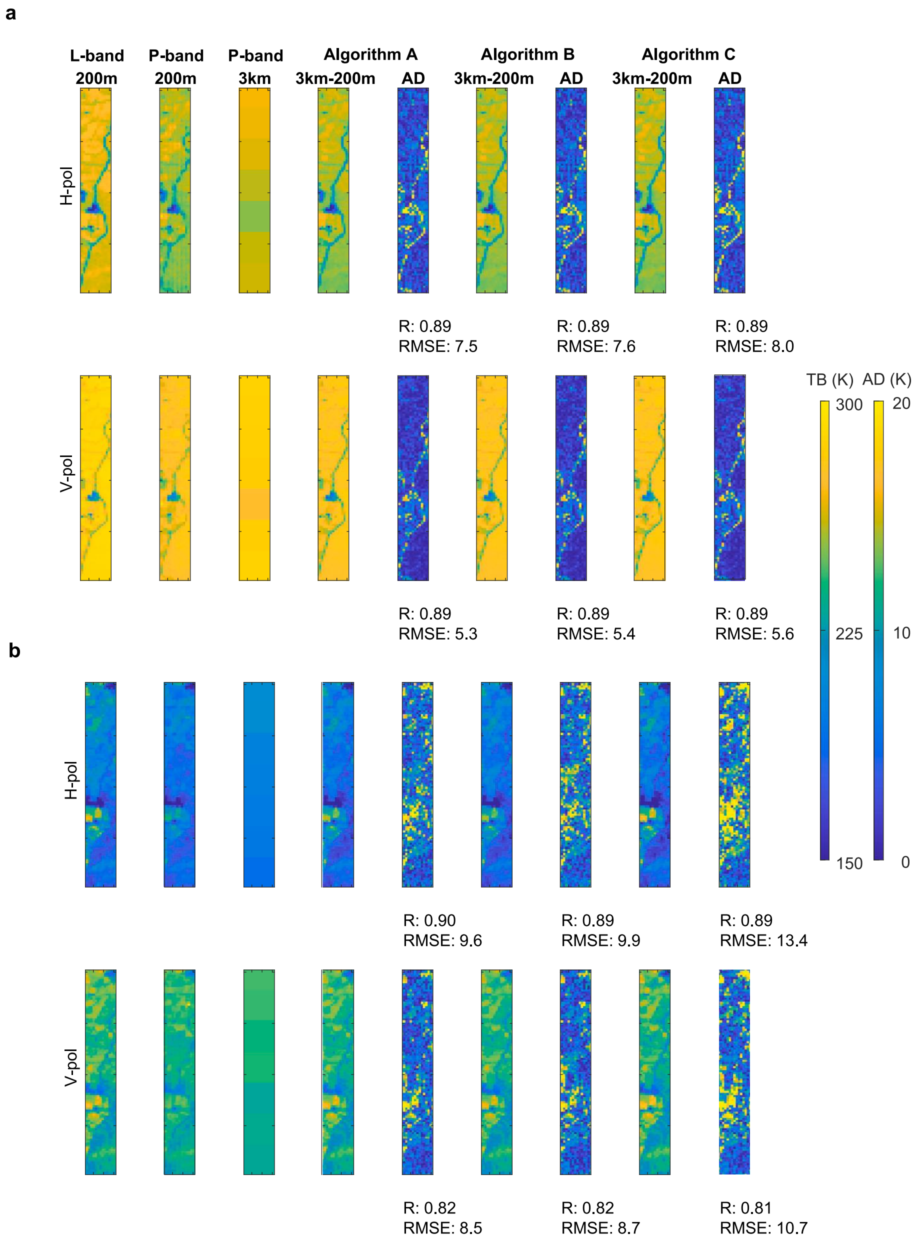

Fig. 6. An example of (a) dry (7 March 2021) and (b) wet (25 March 2021) conditions during PRISM-21 at horizontal (H) and vertical (V) polarization, downscaled from 3 km to 200 m. The three strips to the left side show the original brightness temperature data for L- and P-band at 38.5° and 45° incidence angle respectively with 200 m resolution, and the aggregated P-band at 3 km resolution. The remaining strips represents the downscaled brightness temperature for each algorithm together with the respective absolute difference (*AD*).

The downscaling algorithm referred to here as “Algorithm C" is an alternative approach developed in this paper, with its performance evaluated assuming that the intercept (a) and slope (b) of the linear relationship between frequencies is constant at coarse and medium scale. Algorithm C was inspired by the active-passive baseline downscaling relationship used in SMAP (Entekhabi et al., 2014a), by relating the L- and P-band Tb observations with intercept a and slope b such that at coarse resolution

$$\boldsymbol{TbP_p}(\boldsymbol{C}) = \boldsymbol{a}(\boldsymbol{C}) + \boldsymbol{b}(\boldsymbol{C})^{*}\boldsymbol{TbL_p}(\boldsymbol{C}), \tag{7}$$

and at medium resolution

$$\boldsymbol{TbP_p}(\boldsymbol{M}) = \boldsymbol{a}(\boldsymbol{M}) + \boldsymbol{b}(\boldsymbol{M})^{*}\boldsymbol{TbL_p}(\boldsymbol{M}). \tag{8}$$

As the target is to achieve P-band at medium resolution from the coarse resolution, the equation at medium resolution can be subtracted from the equation at coarse resolution, thus rewriting as

$$\boldsymbol{TbP_p}(\boldsymbol{M}) - \boldsymbol{TbP_p}(\boldsymbol{C}) = \boldsymbol{a}(\boldsymbol{M}) + \boldsymbol{b}(\boldsymbol{M})^{*}\boldsymbol{TbL_p}(\boldsymbol{M}) - \left(\boldsymbol{a}(\boldsymbol{C}) + \boldsymbol{b}(\boldsymbol{C})^{*}\boldsymbol{TbL_p}(\boldsymbol{C})\right). \tag{9}$$

Assuming that the intercept and slope are related by attributes other than scale, the parameters a and b can be assumed scale invariant at local areas, implying

$$\boldsymbol{a}(\boldsymbol{C}) = \boldsymbol{a}(\boldsymbol{M}) \tag{10}$$

$$\boldsymbol{b}(\boldsymbol{C}) = \boldsymbol{b}(\boldsymbol{M}), \tag{11}$$

with the slope b equal to *MVI* (Shi and Li, 2013), resulting in

$$\boldsymbol{MVI} = \frac{\boldsymbol{TbP_V}(\boldsymbol{C}) - \boldsymbol{TbP_H}(\boldsymbol{C})}{\boldsymbol{TbL_V}(\boldsymbol{C}) - \boldsymbol{TbL_H}(\boldsymbol{C})}, \tag{12}$$

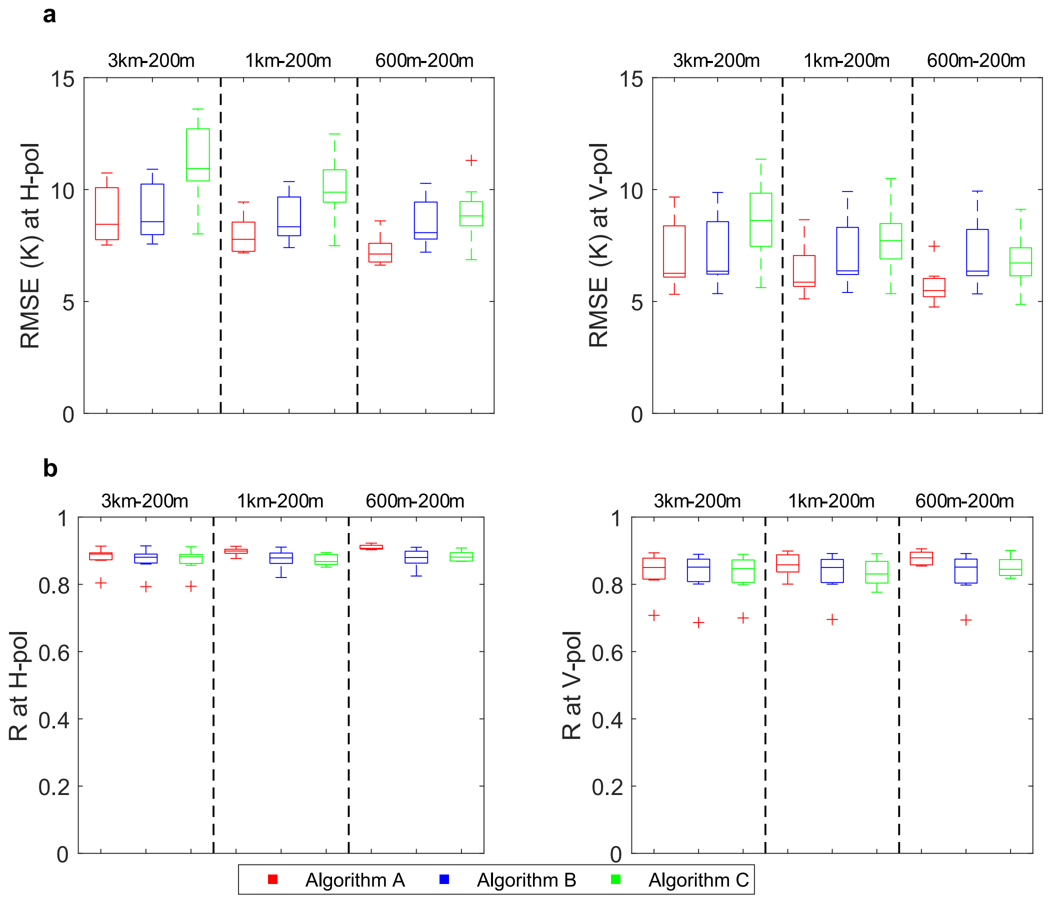

Fig. 7. *RMSE* (a) and *R* (b) performance when downscaling brightness temperature at horizontal polarization (left) and vertical polarization (right) for different resolution combinations (first number is observed resolution and second number is target resolution), using each of the three algorithms during PRISM-21. The box and whiskers represent the variability of *RMSE* and *R* of the whole data set from PRISM-21, including both wet and dry days. The symbol “+” represents the outliers in the statistics.

Table 2
VWC (kg/m^2) from the destructive samples taken during each campaign from the accessible sampling areas. The Almond VWC is an estimation based on the relation of the VWC from a branch sample with the volume of the branch and the volume of the whole tree.

Land Cover Type	PRISM-21	APPLEx-1	APPLEx-2
Wheat/Barely			2.24 ± 1.09
Corn	1.27 ± 0.55		
Cotton	3.95 ± 1.66	5.12 ± 1.70	
Grass	0.05 ± 0.01	0.24 ± 0.17	1.03 ± 0.67
Canola			3.67 ± 2.08
Almond		9.01 ± 7.66	

$$\boldsymbol{TbP_p(M) = TbP_p(C) + MVI^*\left(TbL_p(M) - TbL_p(C)\right)}. \tag{13}$$

For evaluating these three downscaling algorithms, the original observed fine resolution P-band Tb airborne observations, and the aggregated medium resolutions from the original Tb, were then compared with the downscaled estimate using statistics including *RMSE*, correlation coefficient (*R*) and Absolute Difference (*AD*), calculated as

$$\boldsymbol{RMSE} = \sqrt{\frac{\sum_{N=1}^{N}\left(\boldsymbol{Tb_{obs}} - \boldsymbol{Tb_{mod}}\right)^2}{\boldsymbol{N}}}, \tag{14}$$

$$\boldsymbol{R} = \frac{\sum_{N=1}^{N}\left(\left(\boldsymbol{Tb_{mod}} - \overline{\boldsymbol{Tb}}_{\boldsymbol{mod}}\right)^*\left(\boldsymbol{Tb_{obs}} - \overline{\boldsymbol{Tb}}_{\boldsymbol{obs}}\right)\right)}{\sqrt{\sum_{N=1}^{N}\left(\boldsymbol{Tb_{mod}} - \overline{\boldsymbol{Tb}}_{\boldsymbol{mod}}\right)^2}{}^*\sqrt{\sum_{N=1}^{N}\left(\boldsymbol{Tb_{obs}} - \overline{\boldsymbol{Tb}}_{\boldsymbol{obs}}\right)^2}}, \tag{15}$$

$$\boldsymbol{AD} = \left|\boldsymbol{Tb_{obs}} - \boldsymbol{Tb_{mod}}\right|, \tag{16}$$

where $\overline{Tb}$ refers to the mean value of *Tb*, *N* is the number of pixels, the subscript *obs* refers to the observed *Tb* aggregated to the finer resolution, and the subscript mod refers to the model downscaled product.

4. Results

The three passive-passive downscaling methodologies introduced above were analysed based on heterogeneity, downscaling ratio, performance through time, and on the scene spatial variability. APPLEx-1 and PRISM-21 represent drier conditions with some rainfall events between days. Conversely, APPLEx-2 had flooded conditions, with substantially increased flooded area at the end of the campaign. In the case of dry conditions, the soil moisture ranged between 0.01 and 0.15 cm^3/cm^3. Meanwhile, the soil moisture ranged between 0.3 and 0.6 cm^3/cm^3 in the wet conditions. Algorithm B required a linear regression to be developed using the coarse resolution data to attain the parameters required by the downscaling, and so more than one pixel or one instance in time was needed to make this regression. Since the 36 km area represents only one pixel per day, the regression parameters were determined (Fig. 5) using a time-series of observations instead of the spatial variation of observation at an instance in time, as was done for the other resolutions.

Regarding variability in the soil moisture conditions, the three algorithms were assessed by analysing the *AD*. During PRISM-21 (Fig. 6), the dry days or days without a rainfall event showed that the largest

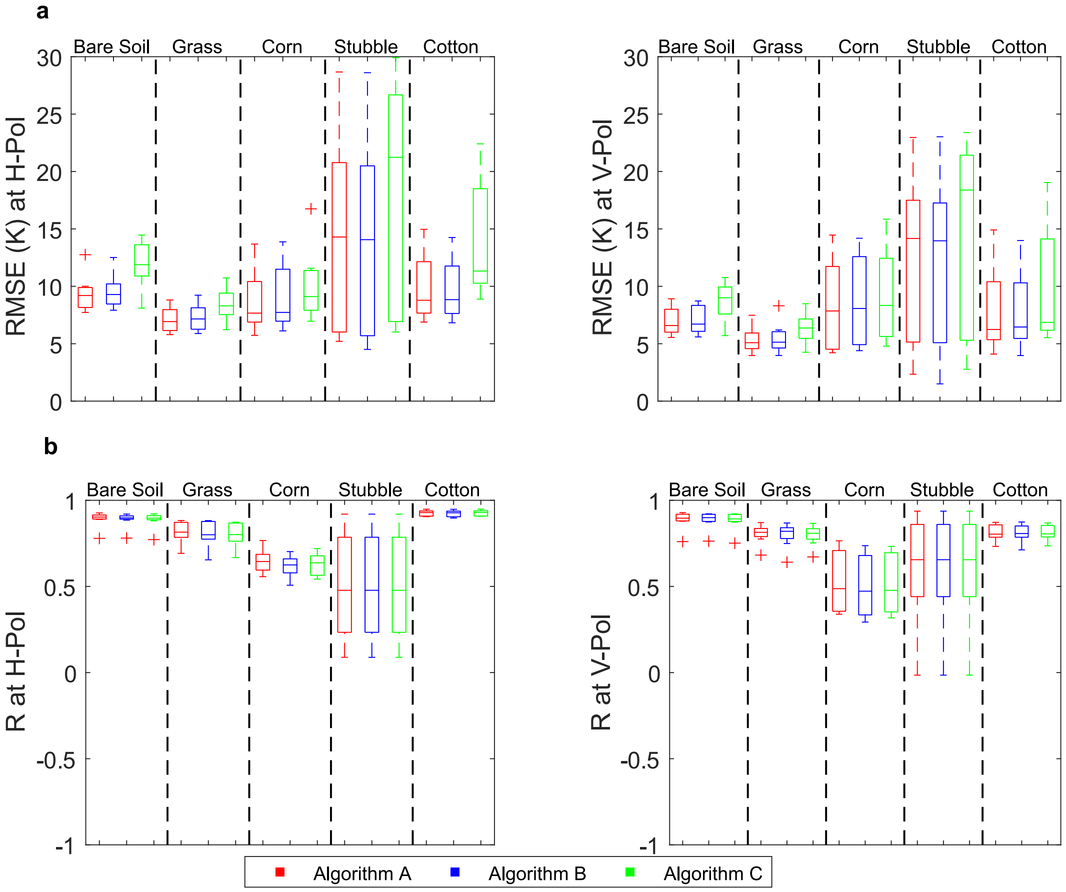

Fig. 8. As for Fig. 6 but at the single downscaling resolution combination of 3 km to 200 m, separated according to each land cover type.

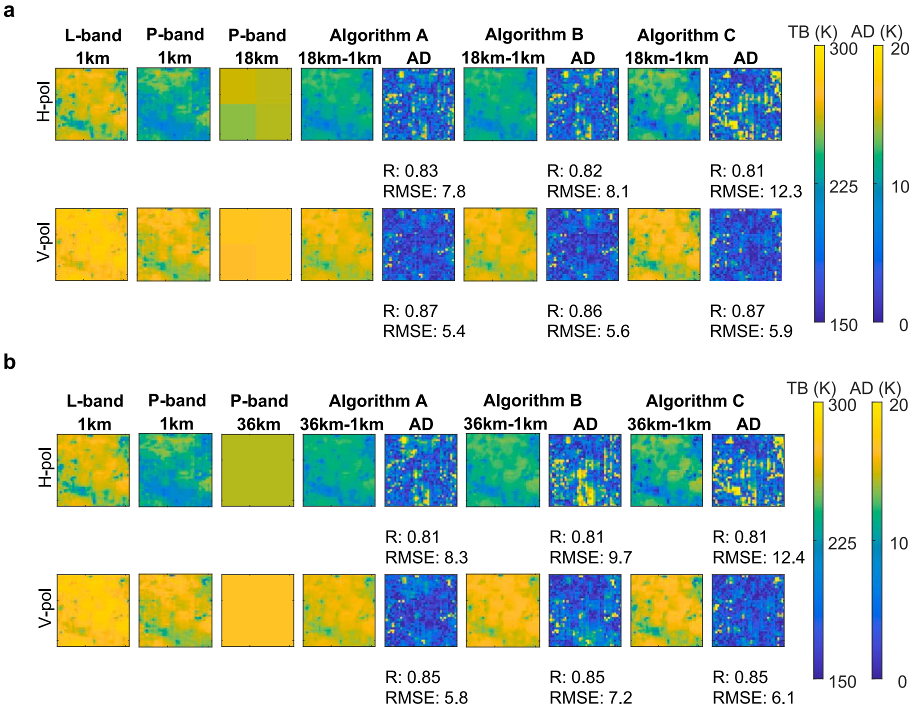

Fig. 9. As for Fig. 6 but for downscaling from 18 km to 1 km (a) and 36 km to 1 km (b) for a dry day (3 February 2022) during APPLEx-1.

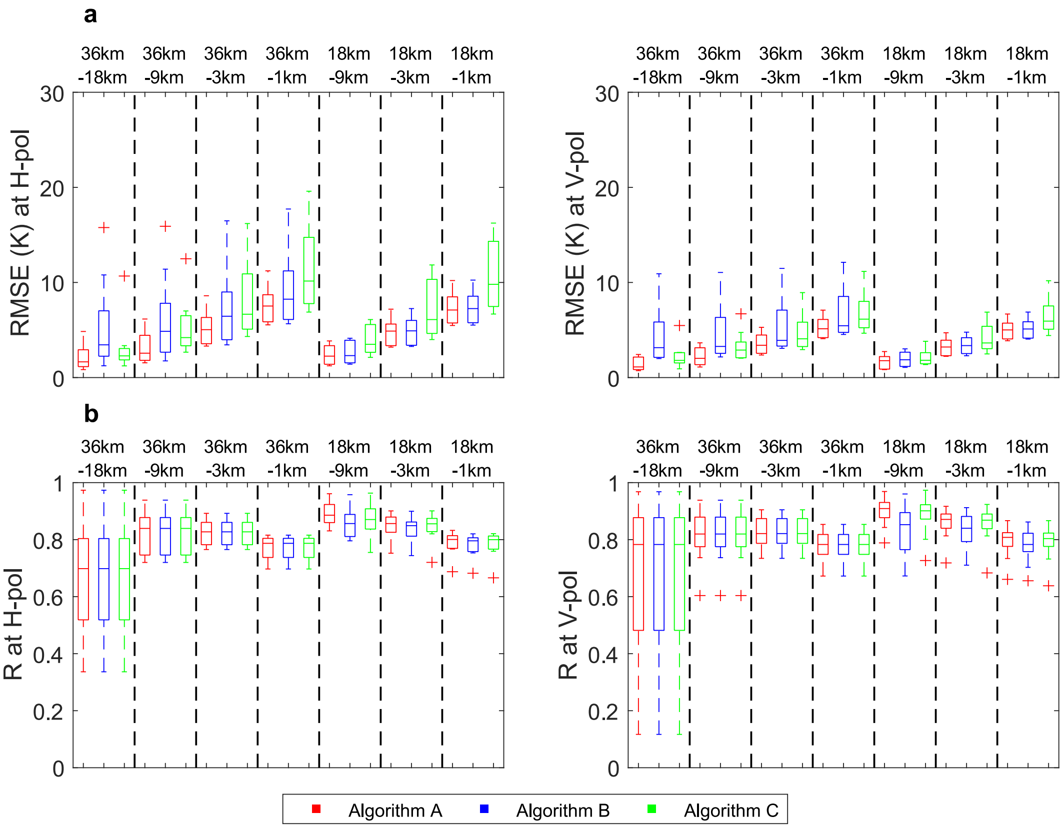

Fig. 10. As for Fig. 7 but during APPLEx-1 with a coarser resolution.

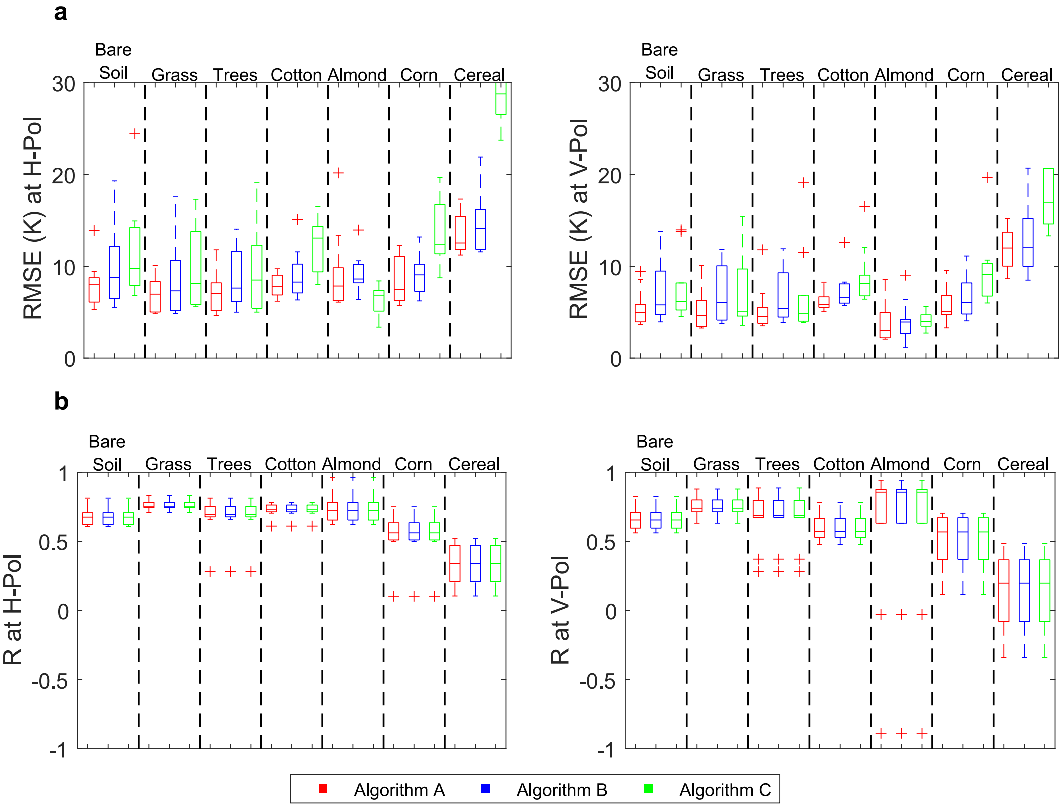

Fig. 11. As for Fig. 8 but for a downscaling resolution combination of 36 km to 1 km during APPLEx-1.

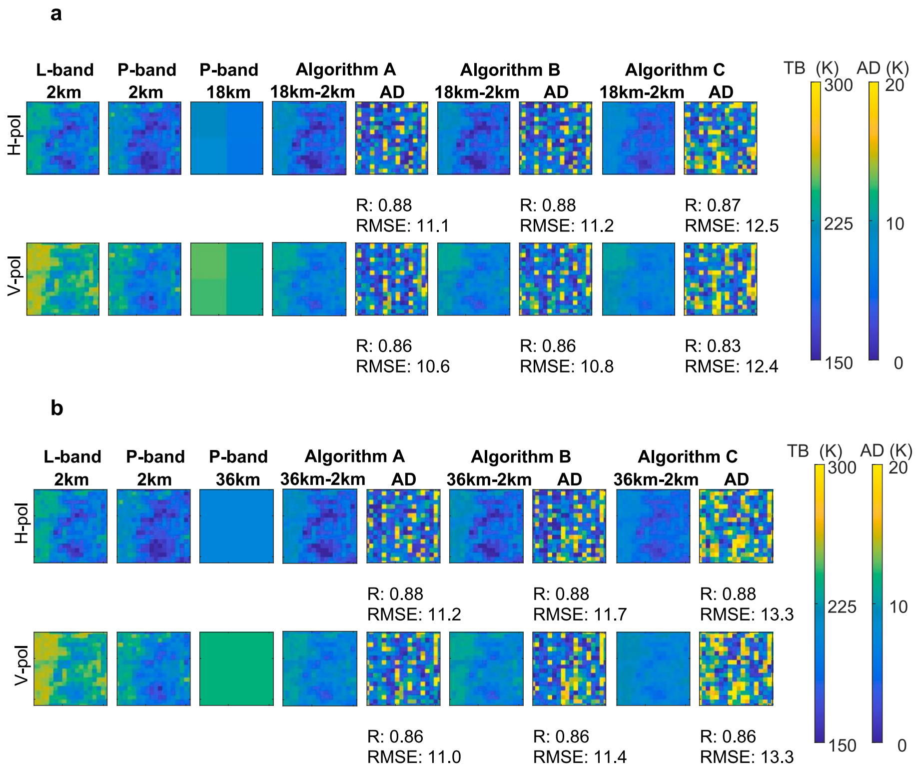

Fig. 12. As for Fig. 6 and Fig. 9 but for downscaling from 18 km to 2 km (a) and 36 km to 2 km (b) for a flooded day (18 October 2022) during APPLEx-2.

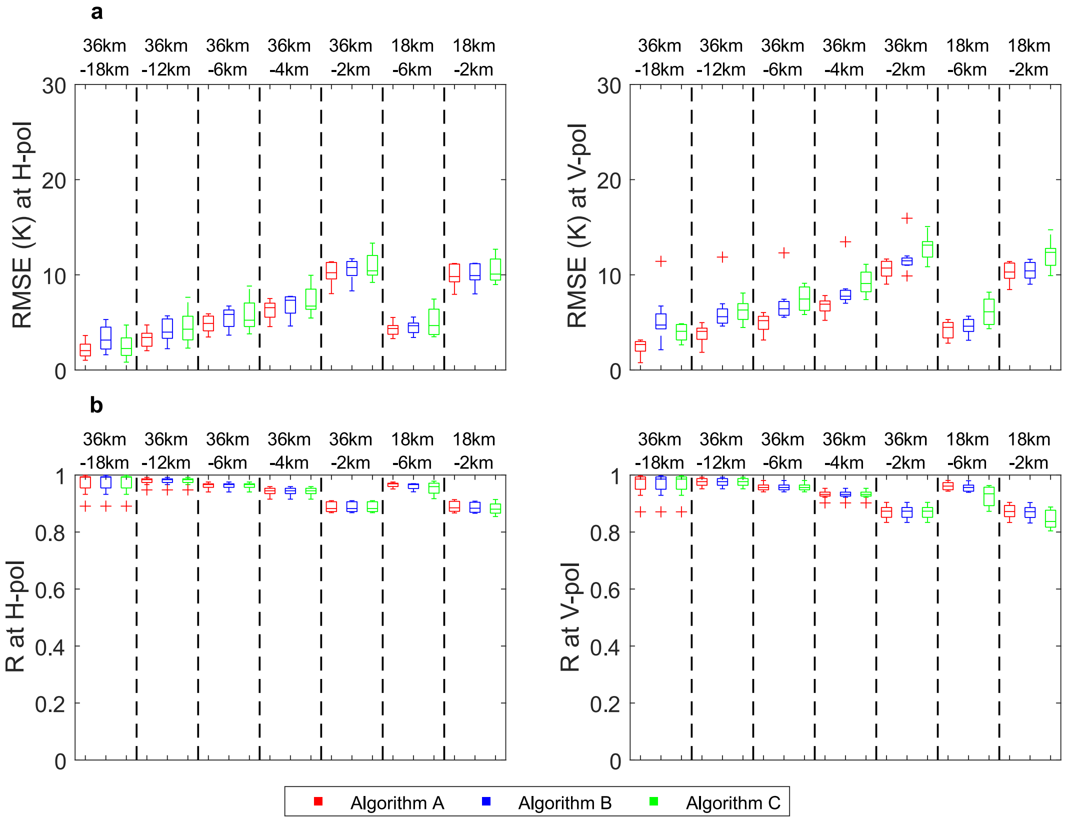

Fig. 13. *RMSE* (a) and R (b) performance when downscaling brightness temperature at horizontal polarization (left) and vertical polarization (right) for different resolution combinations, using each of the three algorithms during APPLEx-2. The box and whiskers represent the variability of *RMSE* and *R* of the whole dataset from APPLEx-2.

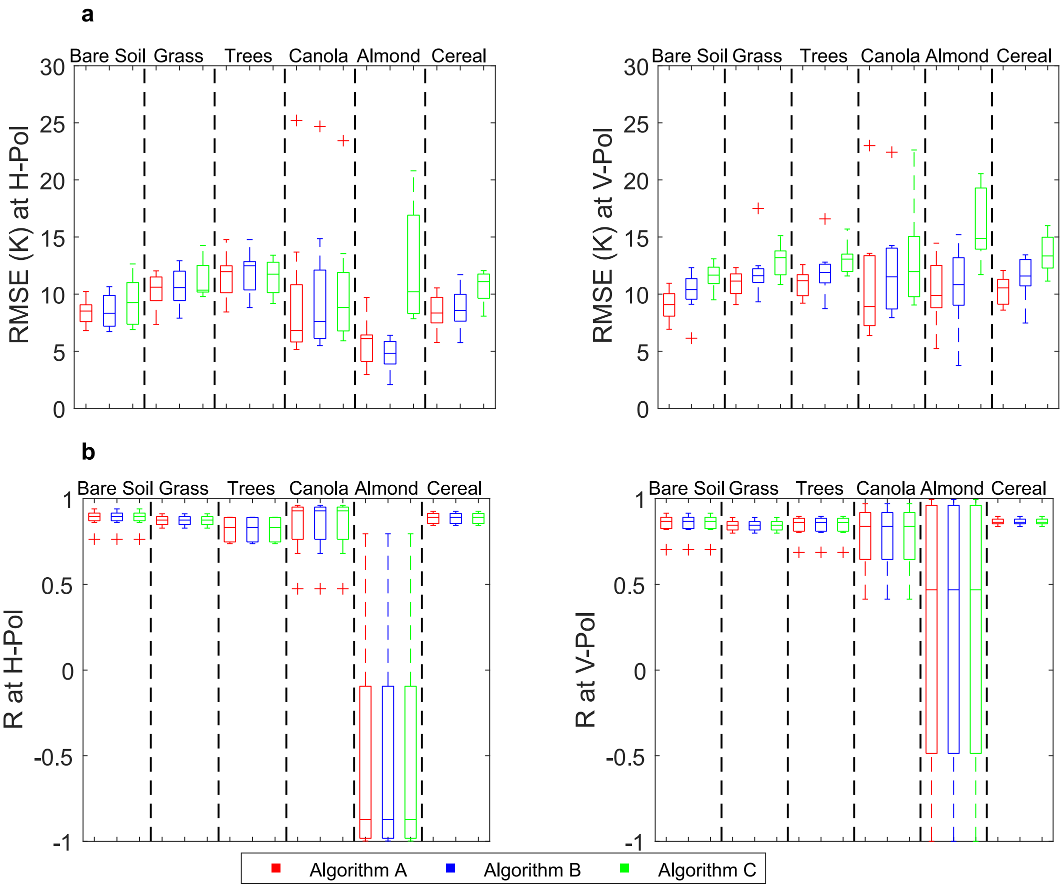

Fig. 14. As for Fig. 8 but for downscaling resolution combination of 36 km to 2 km during APPLEx-2.

errors were located in the vicinity of water bodies and flood irrigated crops, due to the sharp contrast in Tb between the water and land surface features. Algorithm A demonstrated a slightly better performance, with a maximum difference between *RMSE* of Algorithm B and Algorithm C of 0.1 K to 0.5 K, respectively, during the dry condition. For wet days following high precipitation, the higher Tb areas presented a greater *AD* between the downscaled and original P-band Tb values, especially with Algorithm C. This could be contributed to the heterogeneity representation, as those warmer Tb areas also reflected a greater spatial standard deviation in comparison to the rest of the area, and therefore the downscaling from a coarser resolution to a finer resolution resulted in a larger *AD*. Moreover, in contrast with the dry day, the *AD* in the wet day tended to be more spatially variable and not just focussed around water bodies. Consequently, dry days had a better performance than wet days in all three algorithms. Additionally, in both wet and dry conditions, the V polarization was substantially better than H polarization with a difference between 1.1 K to 2.7 K in terms of *RMSE*, but in both cases, the *R* remained approximately equivalent to 0.8. Consequently, the pattern of the downscaled Tb for each algorithm remained quite similar to that from the observed P-band at that resolution for both V and H polarization, but the downscaled V polarization had a closer match to the actual observed Tb values, especially for Algorithm A, with an *RMSE* between 5 K to 10 K (Fig. 7).

When downscaling from increasingly finer resolutions, the performance increased as expected for all three algorithms (Fig. 7). PRISM-21 tended to have an *RMSE* above 5 K, which can be related to the fact that at finer resolution there is more heterogeneity in the observed Tb. Thus, downscaling from 600 m to 200 m had a better performance than from 3 km or 1 km to 200 m, since the 600 m resolution observations better captured the underlying heterogeneity than the observations at 3 km and 1 km.

The land cover conditions for each campaign were different, including the VWC quantity (Table 2), and so the downscaling performance was analysed per these changes. In PRISM-21, the stubble area presented the highest *RMSE* across all three downscaling algorithms (Fig. 8). This could be related to the size of the area covered, since it is relatively small in comparison with other land cover types, and so being neglected in the coarser resolutions. Moreover, the Tb values over that area tended to be lower than adjacent areas, meaning that the associated soil moisture was likely higher due to the lack of actively growing vegetation. Based on the three algorithms and two polarizations within the dataset, the crops showed more variability in the downscaled error. Specifically, corn and cotton had a median and standard deviation in *RMSE* of 8.3 K ± 3.4 K and 8.1 K ± 4.6 K, respectively, having a higher level of *RMSE* variability compared to grass (6.4 K ± 1.6 K) and bare soil (8.6 K ± 2.3 K). The remarkable spatial variability of VWC in cropped areas potentially influenced the spatial variability in Tb, which the downscaling was unable to capture.

During APPLEx-1, Algorithm A had a better performance than the other two algorithms (Fig. 9). It can be seen within the spatial pattern of Tb that the *AD* increased over areas where P-band tended to be colder than L-band, especially at H polarization, and is most obvious for the downscaling from 36 km resolution with Algorithm B in the south of the area. However, when downscaling from 18 km resolution, the discrepancies in the patterns reduced. Importantly, using data from adjacent days to retrieve Algorithm B parameters may have contributed to a reduced correlation between L- and P-band Tb in some areas where the downscaling was from 36 km. Additionally, considering the predominantly dry conditions in APPLEx-1, similarly to PRISM-21, the V polarization had the greatest *AD* values in areas containing water bodies and/or days with flood irrigation.

It was noted in APPLEx-1, that when downscaling from 36 km, the

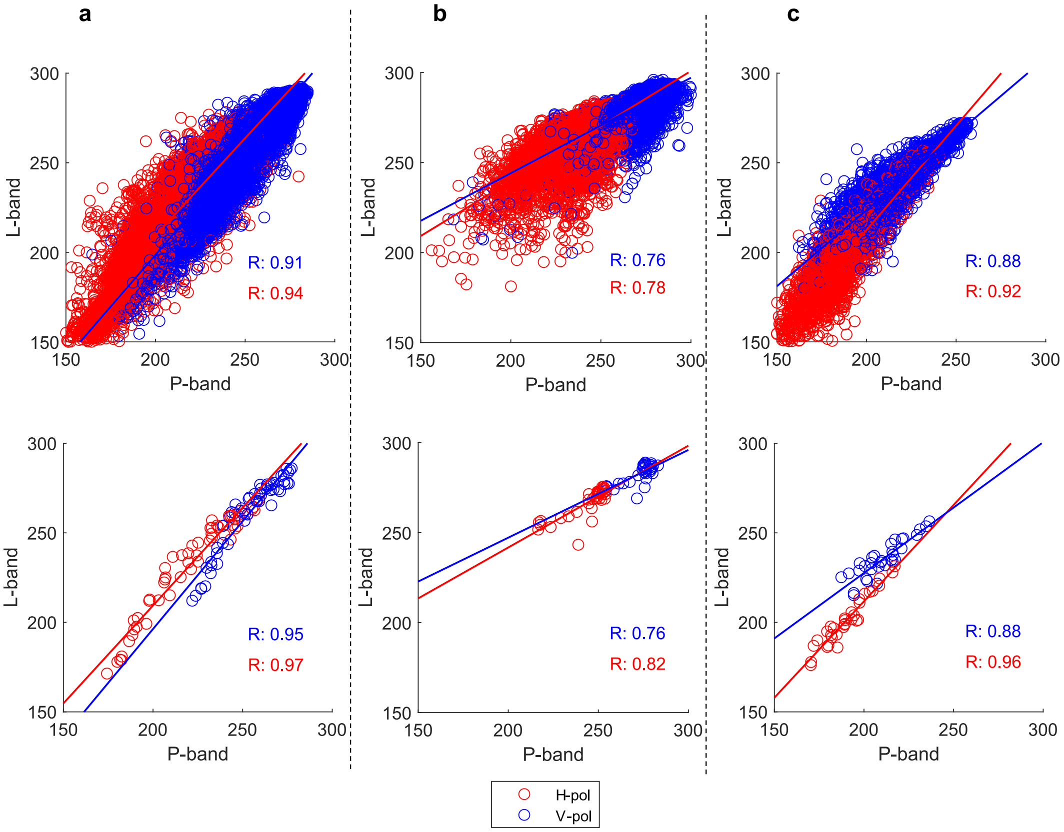

Fig. 15. Relationship between original observed L- and P-band data at finer (top row) and coarser (bottom row) resolutions. (a) PRISM-21 at 200 m (top row) and 3 km (bottom row) resolution, (b) APPLEx-1 at 1 km (top row) and 18 km (bottom row) resolution, and (c) APPLEx-2 at 2 km (top row) and 18 km (bottom row) resolution. The red and blue line represents the linear fit at H and V polarization. (For interpretation of the references to colour in this figure legend, the reader is referred to the web version of this article.)

three algorithms had a similar performance across scales in terms of *R*, and with decreased *R* by downscaling to an increasingly finer resolution (Fig. 10). This may be due to the fact that the downscaling was made from only one pixel covering an area of 36 km × 36 km, but as more pixels were used, as shown for the 18 km resolution, Algorithm A tended to have a slightly better R than the other algorithms, reflecting a more similar spatial pattern in comparison with the observed P-band Tb. In addition, Algorithm B had considerably greater variability in the error when downscaling from 36 km resolution than from 18 km resolution. As there were more dry days than wet days, the given set of parameters were unsuitable for every condition. Therefore, Algorithm B had a better performance when the parameter regression was done spatially as shown in the 18 km downscaling, than when done through time as in the 36 km downscaling. Moreover, the *RMSE* increased when the downscaling was made from a coarser to an increasingly finer resolution in both polarizations. Accordingly, not all the heterogeneity can be well represented when going to a finer resolution, thus resulting in more error. For instance, when the resolution was increased from 36 km to 18 km, the median and standard deviation error from both polarization datasets combined resulted in Algorithm A having an error of 1.3 K ± 1.1 K, Algorithm B of 3.3 K ± 4.0 K, and Algorithm C of 2.2 K ± 2.2 K. However, when the downscaling was performed from 36 km to 1 km resolution the error increased to 5.9 K ± 2.0 K, 6.8 K ± 3.7 K, and 7.6 K ± 4.2 K for Algorithm A, B and C respectively.

Land cover types including grass and trees tended to have a similar median *RMSE* in the three algorithms during APPLEx-1 (Fig. 11). This could be related to the fact that the trees are in an open woodland setting, exposing a substantial amount of grass in between the sparse distribution of trees. Consequently, a resolution finer than 1 km may be needed to detect a performance difference between grass and tree landcover. Conversely, the dry weather conditions and the low VWC in the grass could result in a similar performance between the bare soil and the grass. However, in terms of algorithm performance, Algorithm A was found to be slightly better and more robust than Algorithm B and C for these two land cover types. Most of the error and lack of pattern agreement was in the cereal crops, having the worst results when downscaling using Algorithm C. One reason is that this area is sparse and so not prominent during APPLEx-1, with its heterogeneity representation diminished or not fully captured in coarser resolutions. Moreover, some of the areas seemingly had wet/irrigated conditions due to their low Tb, where Algorithm C demonstrated most of the error.

In APPLEx-2, the eastern half of the study area (see Fig. 2) was less affected by the flooded conditions than the western half. In both areas, Algorithm C tended to have the least agreement with the observed Tb in comparison with the other two algorithms (Fig. 12). It is noted that the coldest Tb pixel values presented a low downscaling performance, especially by Algorithm C with *RMSE* of 12.11 K for V polarization and 13.03 K for H polarization when downscaling from 36 km to 2 km resolution, inferring that the partially flooded areas could not be well represented. Moreover, in the three algorithms, the warmest Tb regions tended to be diminished in the downscaling result. Notably, the *RMSE* error increased by 0.1 K to 0.9 K when the downscaling was made from 36 km to 2 km in comparison with the downscaling from 18 km to 2 km resolution. Accordingly, the downscaling needed to be undertaken from a higher resolution to capture those small warmer areas, which were surrounded mostly by flooded conditions.

Algorithm A had better performance than the other two algorithms for both polarizations during flooded conditions (Fig. 13). Here the error had a median value of around 10 K when downscaling from 36 km to 2 km, reducing to around 3 K when downscaling from 36 km to 18 km. In

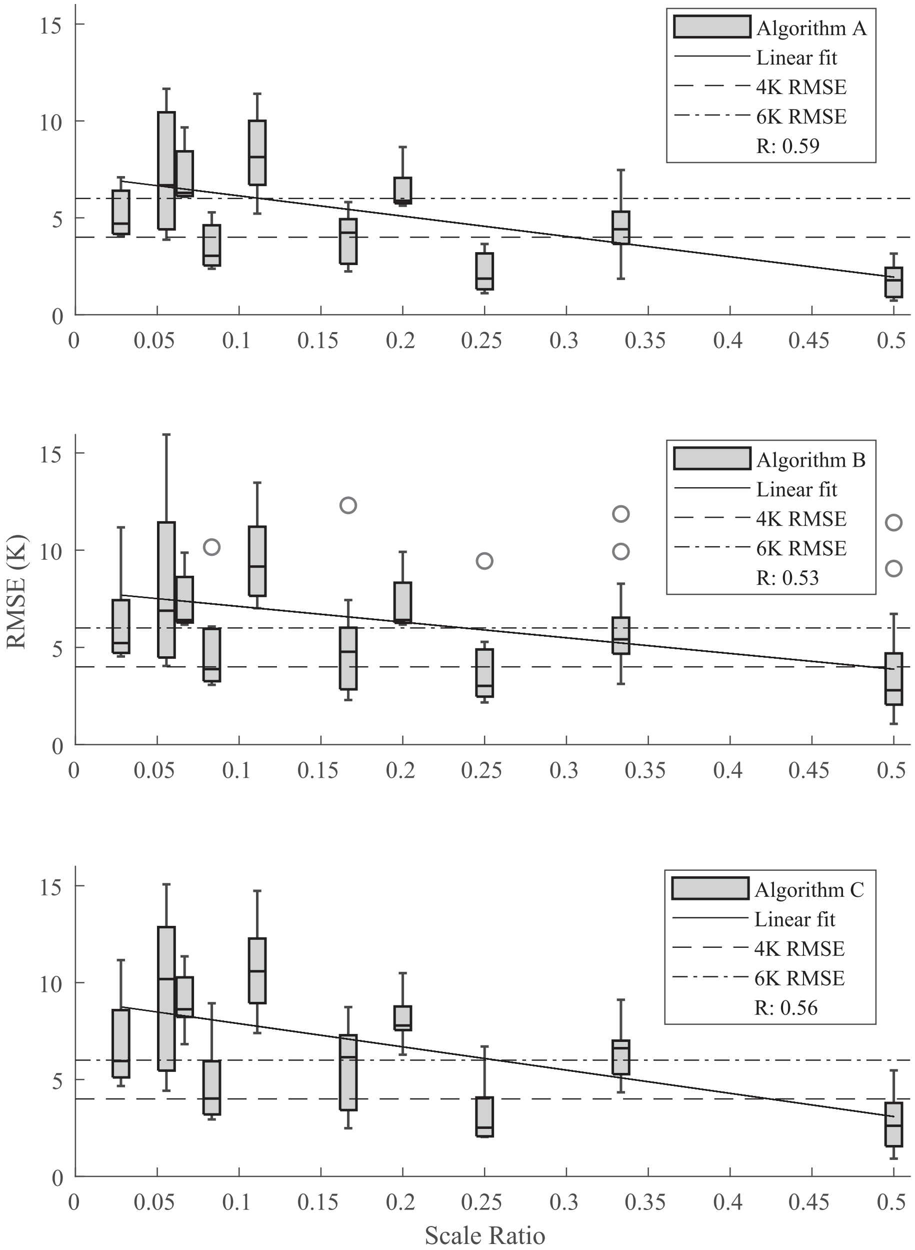

Fig. 16. *RMSE* for each algorithm across all three campaigns at V polarization, compared against the scale ratio, defined as ratio of the downscaled to original resolution. The R is calculated between the fitted line and the median. The box and whiskers represent the variability of *RMSE* within the three campaigns, while the circles are outliers. The dashed and dot-dashed lines represent error targets.

general, as the downscaling was made from a coarser resolution to an increasingly finer resolution the performance decreased, with the performance being further reduced for flooded conditions when compared with dry days.

The performance for each land cover type was impacted by the flooding conditions, as shown clearly by the almond crop (Fig. 14). Algorithm C was most affected as it cannot represent well the pattern of the observed Tb value for ponded areas. Among the other crops in APPLEx-2, the canola displayed more variability in *RMSE* and *R*, which could be related to more notable differentiation of spatial VWC than the other crops, reflected in the spread of Tb values and the greater variability in the downscaling performance.

5. Discussion

To demonstrate the correlation between L- and P-band, Fig. 15 shows a scatter plot of both Tb observations at the same spatial resolutions. A linear agreement between L- and P-band is clearly seen, being most obvious in the coarser observations. The greater variability at the finer resolutions is likely influenced by the spatial heterogeneity of land surface conditions and potential variation in the sensing depth of the observations for the two frequencies, along with effects from angle normalization of the data and not being at exactly the same incidence angles. Consequently, this impacts the passive-passive L- and P-band downscaling linear model performance as it goes to a finer resolution. Moreover, the correlation tended to be stronger in H polarization than in V polarization in this relationship.

An analysis of scale ratio between the original coarse Tb and the downscaled resolution was assessed to determine the expected *RMSE* for each algorithm at V and H polarization, and thus the maximum resolution enhancement that could be undertaken within a target accuracy specification. Accordingly, this analysis incorporated the data from all

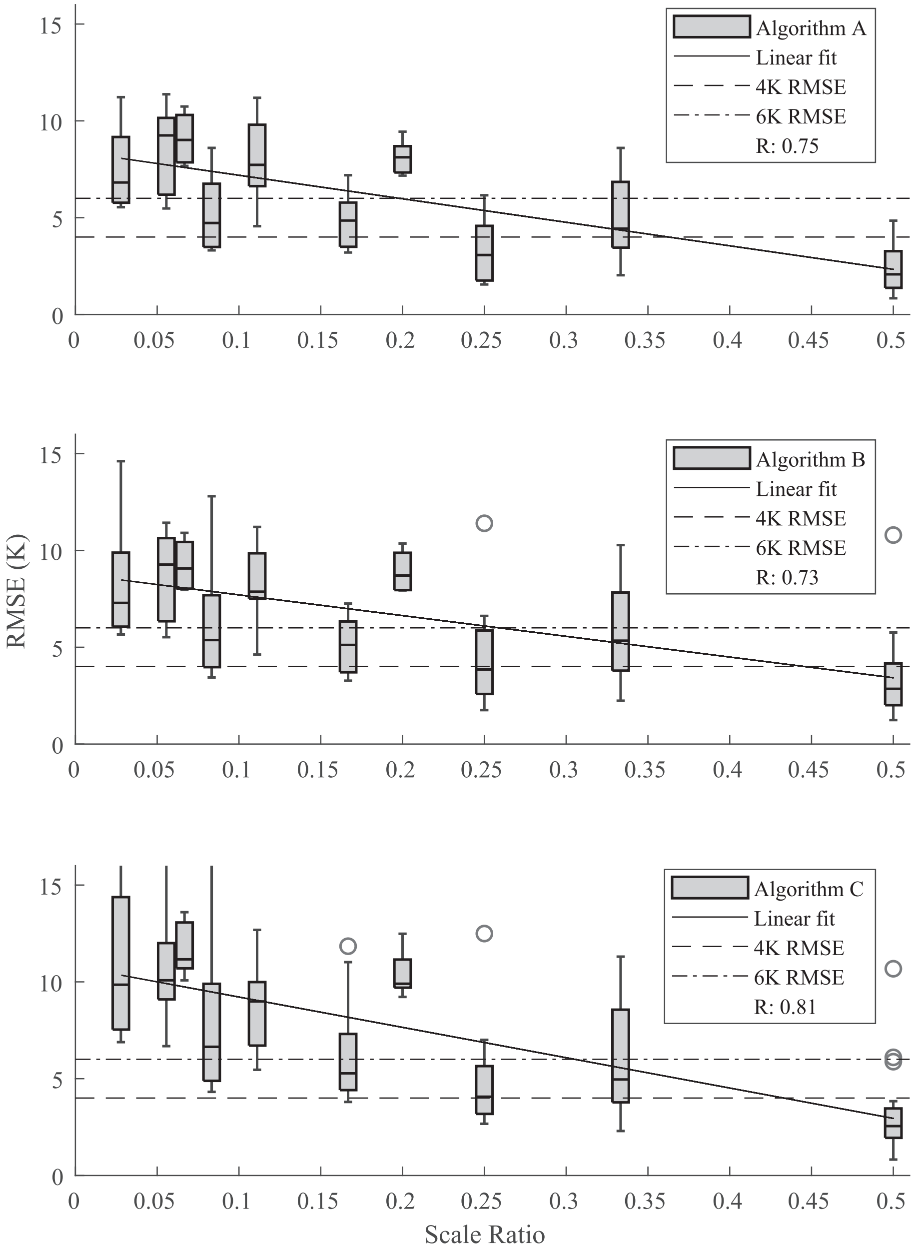

Fig. 17. As for Fig. 16 but for H polarization.

three of the campaigns (Fig. 16 and Fig. 17). At V polarization, Algorithm A achieved an *RMSE* of 4 K and 6 K for scale ratios of around 0.31 and 0.12 respectively. Meanwhile, at H polarization the same expected *RMSE* range was able to execute a downscaling scale ratio between 0.36 and 0.20. Conversely, Algorithm C showed the poorest performance at smaller ratios in both polarizations than Algorithm B and A. Moreover, the performance fluctuated between Algorithm C and B once the scale ratio increased beyond approximately 0.25. Therefore, Algorithm C could achieve a similar general performance with Algorithm B at around one-quarter of the initial observed resolution, but the Algorithm C performance decreased at lower downscaling ratios in comparison with the other two algorithms. Thus, Algorithm A could represent more heterogeneity when downscaling from coarser to finer scales than Algorithms B and C, particularly at V polarization. In addition, across the three campaigns, the *R* between the downscaled and observed P-band Tb was around 0.8 irrespective of the algorithm or scale ratio. Consequently, the three algorithms followed a similar pattern as the observed Tb, but the corresponding observed value was represented differently by that predicted from each algorithm.

From the three campaigns, it is clear that in wet conditions the performance reduced in comparison to dry days. In addition, this performance further decreased when encountering predominant spatial changes in VWC as noticed in crops like canola, cotton, and cereal. Moreover, the size of the area covered by each crop determined its influence on the downscaling result. For instance, when cereal was more extensive in area, such as in APPLEx-2 with 184.5 km^2 than in APPLEx-1 with 10.5 km^2, the *RMSE* decreased comparatively. Furthermore, in small areas with flooding or ponded water, the error also increased, impacting Algorithm C in particular. The performance of the bare soil area behaved similarly to grass areas during the APPLEx campaigns, but in PRISM-21 the *RMSE* was slightly larger, associated with heterogeneity due to variations in roughness conditions.

6. Conclusion

This paper aimed to find the best approach for enhancing the spatial resolution of P-band Tb by using higher resolution L-band Tb, considering different land cover and moisture conditions. In general, the SFIM approach, referred to as Algorithm A in this paper, performed best in comparison with the other two algorithms, especially for V polarization. A median *RMSE* of approximately 3 K was achieved when downscaling from 36 km to 18 km, being better than the performance required for Tb input for soil moisture retrieval. Accordingly, as long as a 0.5 resolution ratio is needed, Tb data at P-band can be downscaled with an accuracy better than 3 K. However, for future satellite missions such as Cryorad that will allow a resolution ratio of 0.2, the expected error can increase to around 5 K, allowing the retrieval of RZSM from P-band or/and L- and P-band together at a higher resolution. When downscaling from coarser resolution to an increasingly finer resolution the performance degraded, being related to spatial heterogeneity. In dry periods, the downscaling accuracy of the three algorithms was relatively improved in comparison to wet periods. Moreover, predominantly cold Tb conditions were found to mask small warm areas when downscaling from a coarse resolution. Finally, in cropped areas, the performance was found to be affected by the spatial variation in VWC dynamics.

CRediT authorship contribution statement

Luisa F. White-Murillo: Writing – original draft, Methodology, Investigation, Formal analysis, Data curation. **Jeffrey P. Walker:** Writing – review & editing, Supervision, Formal analysis, Conceptualization. **Nan Ye:** Writing – review & editing, Supervision, Data curation, Conceptualization. **James Hills:** Writing – review & editing, Supervision, Conceptualization. **Xiaoling Wu:** Writing – review & editing, Project administration, Data curation. **Lixiaozhou Zhou:** Resources, Project administration, Data curation. **Ziwei Xiong:** Resources, Project administration, Data curation. **Liujun Zhu:** Project administration, Data curation, Conceptualization. **Brian Ng:** Writing – review & editing, Supervision, Project administration, Conceptualization. **Mahta Moghaddam:** Supervision, Project administration, Conceptualization. **Simon Yueh:** Supervision, Project administration, Conceptualization.

Declaration of competing interest

The authors declare the following financial interests/personal relationships which may be considered as potential competing interests:

Luisa F. White-Murillo reports financial support was provided by Monash University. Jeffrey P. Walker reports financial support was provided by Australian Research Council. If there are other authors, they declare that they have no known competing financial interests or personal relationships that could have appeared to influence the work reported in this paper.

Acknowledgments

This work has been possible due to the volunteers who helped acquire the associated data of the PRISM21, APPLEx-1, and APPLEx-2 campaigns. The Monash personnel, Pascal Mater, Kiri Mason, John Beadle, and Les Bugajski, who prepared and maintained instrumentation prior to and throughout the field campaigns are also acknowledged. Data used in this project was financed through Australian Research Council Discovery Projects DP210100430, DP170102373, Linkage Infrastructure, Equipment, and Facilities Grants LE190100045, LE150100047, LE0882509, and LE0453434. Postgraduate Scholarships were funded by DP210100430, Monash Civil Engineering Department, and Monash Faculty of Engineering.

Data availability

Data will be made available on request.

References

Ahmad, A., Quegan, S., 2012. Analysis of maximum likelihood classification technique on Landsat 5 TM satellite data of tropical land covers. In: Proceedings - 2012 IEEE International Conference on Control System, Computing and Engineering, ICCSCE 2012. IEEE Computer Society, pp. 280–285. https://doi.org/10.1109/ICCSCE.2012.6487156.

Brakhasi, F., Walker, J.P., Ye, N., Wu, X., Shen, X., Yeo, I.-Y., Boopathi, N., Kim, E., Kerr, Y., Jackson, T., 2023. Towards soil moisture profile estimation in the root zone using L- and P-band radiometer observations: a coherent modelling approach. Sci. Remote Sens. 7, 100079. https://doi.org/10.1016/J.SRS.2023.100079.

Brakhasi, F., Walker, J.P., Judge, J., Liu, P.W., Shen, X., Ye, N., Wu, X., Yeo, I.Y., Boopathi, N., Kim, E., Kerr, Y.H., Jackson, T.J., 2024a. A comparison of passive microwave emission models for estimating brightness temperature at L- and P-bands under bare and vegetated soil conditions. IEEE J. Sel. Top. Appl. Earth Obs. Remote Sens. 17, 2570–2585. https://doi.org/10.1109/JSTARS.2023.3344764.

Brakhasi, F., Walker, J.P., Judge, J., Liu, P.W., Shen, X., Ye, N., Wu, X., Yeo, I.Y., Kim, E., Kerr, Y., Jackson, T., 2024b. Soil moisture profile estimation under bare and vegetated soils using combined L-band and P-band radiometer observations: an incoherent modeling approach. Remote Sens. Environ. 307, 114148. https://doi.org/10.1016/j.rse.2024.114148.

Calvet, J.C., Wigneron, J.P., Walker, J., Karbou, F., Chanzy, A., Albergel, C., 2011. Sensitivity of passive microwave observations to soil moisture and vegetation water content: L-band to W-band. IEEE Trans. Geosci. Remote Sens. 49, 1190–1199. https://doi.org/10.1109/TGRS.2010.2050488.

Entekhabi, D., Njoku, E.G., O'Neill, P.E., Kellogg, K.H., Crow, W.T., Edelstein, W.N., Entin, J.K., Goodman, S.D., Jackson, T.J., Johnson, J., Kimball, J., Piepmeier, J.R., Koster, R.D., Martin, N., McDonald, K.C., Moghaddam, M., Moran, S., Reichle, R., Shi, J.C., Spencer, M.W., Thurman, S.W., Tsang, L., Van Zyl, J., 2010. The soil moisture active passive (SMAP) mission. Proc. IEEE 98, 704–716. https://doi.org/10.1109/JPROC.2010.2043918.

Engman, E.T., Chauhan, N., 1995. Status of microwave soil moisture measurements with remote sensing. Remote Sens. Environ. 51, 189–198. https://doi.org/10.1016/0034-4257(94)00074-W.

Entekhabi, D., Das, N., Njoku, E., Yueh, S., Johnson, J., Shi, J., 2014a. Soil moisture active passive (SMAP) algorithm theoretical basis document L2 & L3 radar/radiometer soil moisture (active/passive) data products. Jet propulsion laboratory.

Entekhabi, D., Yueh, S., O'Neill, P.E., Kellogg, K.H., Allen, A., Bindlish, R., Brown, M., Chan, S., Colliander, A., Crow, W.T., Das, N., De Lannoy, G., Dunbar, R.S., Edelstein, W.N., Entin, J.K., Escobar, V., Goodman, S.D., Jackson, T.J., Jai, B., Johnson, J., Kim, E., Kim, S., Kimball, J., Koster, R.D., Leon, A., McDonald, K.C., Moghaddam, M., Mohammed, P., Moran, S., Njoku, E.G., Piepmeier, J.R., Reichle, R., Rogez, F., Shi, J.C., Spencer, M.W., Thurman, S.W., Tsang, L., Van Zyl, J., Weiss, B., West, R., 2014b. SMAP handbook soil moisture active passive. In: Mapping Soil Moisture and Freeze/Thaw from Space, Jet Propulsion Laboratory. California Institute of Technology. National Aeronautics and Space Administration.

Escorihuela, M.J., Chanzy, A., Wigneron, J.P., Kerr, Y.H., 2010. Effective soil moisture sampling depth of L-band radiometry: a case study. Remote Sens. Environ. 114, 995–1001. https://doi.org/10.1016/j.rse.2009.12.011.

Jackson, R.B., Canadell, J., Ehleringer, J.R., Mooney, H.A., Sala, O.E., Schulze, E.D., 1996. A global analysis of root distributions for terrestrial biomes. Oecologia 108, 389–411. https://doi.org/10.1007/BF00333714.

Kerr, Y.H., Waldteufel, P., Wigneron, J.P., Martinuzzi, J.M., Font, J., Berger, M., 2001. Soil moisture retrieval from space: the soil moisture and ocean salinity (SMOS) mission. IEEE Trans. Geosci. Remote Sens. 39, 1729–1735. https://doi.org/10.1109/36.942551.

Kerr, Y.H., Waldteufel, P., Wigneron, J.P., Delwart, S., Cabot, F., Boutin, J., Escorihuela, M.J., Font, J., Reul, N., Gruhier, C., Juglea, S.E., Drinkwater, M.R., Hahne, A., Martin-Neira, M., Mecklenburg, S., 2010. The SMOS Mission: new tool for monitoring key elements of the global water cycle. Proc. IEEE 98, 666–687. https://doi.org/10.1109/JPROC.2010.2043032.

Le Vine, D.M., Wilheit, T.T., Murphy, R.E., Swift, C.T., 1989. A multifrequency microwave radiometer of the future. IEEE Trans. Geosci. Remote Sens. 27, 193–199. https://doi.org/10.1109/36.20298.

Li, L., Sun, J., Zhang, F., Guo, T., Bao, X., Smith, F.A., Smith, S.E., 2006. Root distribution and interactions between intercropped species. Oecologia 147, 280–290. https://doi.org/10.1007/s00442-005-0256-4.

Liu, J.G., 2000. Smoothing filter-based intensity modulation: a spectral preserve image fusion technique for improving spatial details. Int. J. Remote Sens. 21, 3461–3472. https://doi.org/10.1080/014311600750037499.

Lu, Hanyu, He, Q., Zhao, T., Yao, P., Peng, Z., Lu, T., Lu, Haishen, 2022. An intercomparison study of algorithms for SMAP brightness temperature resolution enhancement with or without information from AMSR2. IEEE J. Sel. Top. Appl. Earth Obs. Remote Sens. 15, 2058–2069. https://doi.org/10.1109/JSTARS.2022.3152506.

Macelloni, G., Brogioni, M., Leduc-Leballeur, M., Montomoli, F., Bartsch, A., Mialon, A., Ritz, C., Closa Soteras, J., Stammer, D., Picard, G., De Carolis, G., Boutin, J., Johnson, J.T., Nicholls, K.W., Jezek, K.C., Rautiainen, K., Kaleschke, L., Bertino, L., Tsang, L., Van Den Broeke, M., Skou, N., Tietsche, S., 2018. Cryorad: A low frequency wideband radiometer mission for the study of the cryosphere. In: Int. Geosci. Remote Sens. Symp. 2018-July, 1998–2000. https://doi.org/10.1109/IGARSS.2018.8519172.

Merlin, O., Escorihuela, M.J., Mayoral, M.A., Hagolle, O., Al Bitar, A., Kerr, Y., 2013. Self-calibrated evaporation-based disaggregation of SMOS soil moisture: an evaluation study at 3km and 100m resolution in Catalunya, Spain. Remote Sens. Environ. 130, 25–38. https://doi.org/10.1016/J.RSE.2012.11.008.

O'Neill, P., Bindlish, R., Chan, S., Chaubell, J., Colliander, A., Njoku, E., Jackson, T., 2021. Algorithm Theoretical Basis Document Level 2 & 3 Soil Moisture (Passive) Data Products. Jet Propuls. Lab.

Peng, J., Albergel, C., Balenzano, A., Brocca, L., Cartus, O., Cosh, M.H., Crow, W.T., Dabrowska-Zielinska, K., Dadson, S., Davidson, M.W.J., de Rosnay, P., Dorigo, W., Gruber, A., Hagemann, S., Hirschi, M., Kerr, Y.H., Lovergine, F., Mahecha, M.D., Marzahn, P., Mattia, F., Musial, J.P., Preuschmann, S., Reichle, R.H., Satalino, G., Silgram, M., van Bodegom, P.M., Verhoest, N.E.C., Wagner, W., Walker, J.P., Wegmüller, U., Loew, A., 2021. A roadmap for high-resolution satellite soil moisture applications – confronting product characteristics with user requirements. Remote Sens. Environ. 252, 112162. https://doi.org/10.1016/J.RSE.2020.112162.

Sabaghy, S., Walker, J., Renzullo, L., Akbar, R., Chan, S., Chaubell, J., Das, N., Dunbar, R. S., Entekhabi, D., Gevaert, A., Jackson, T., Merlin, O., Moghaddam, M., Peng, J., Piepmeier, J., Piles, M., Portal, G., Rudiger, C., Stefan, V., Wu, X., Ye, N., Yueh, S., 2017. Comparison of downscaling techniques for high resolution soil moisture mapping. In: Int. Geosci. Remote Sens. Symp. 2017-July, 2523–2526. https://doi.org/10.1109/IGARSS.2017.8127508.

Sabaghy, S., Walker, J.P., Renzullo, L.J., Akbar, R., Chan, S., Chaubell, J., Das, N., Dunbar, R.S., Entekhabi, D., Gevaert, A., Jackson, T.J., Loew, A., Merlin, O., Moghaddam, M., Peng, Jian, Peng, Jinzheng, Piepmeier, J., Rüdiger, C., Stefan, V., Wu, X., Ye, N., Yueh, S., 2020. Comprehensive analysis of alternative downscaled soil moisture products. Remote Sens. Environ. 239, 111586. https://doi.org/10.1016/j.rse.2019.111586.

Seneviratne, S.I., Corti, T., Davin, E.L., Hirschi, M., Jaeger, E.B., Lehner, I., Orlowsky, B., Teuling, A.J., 2010. Investigating soil moisture–climate interactions in a changing climate: a review. Earth-Sci. Rev. 99, 125–161. https://doi.org/10.1016/J.EARSCIREV.2010.02.004.

Shen, X., Walker, J.P., Ye, N., Wu, X., Boopathi, N., Yeo, I.Y., Zhang, L., Zhu, L., 2021. Soil moisture retrieval depth of P- And L-Band radiometry: predictions and observations. IEEE Trans. Geosci. Remote Sens. 59, 6814–6822. https://doi.org/10.1109/TGRS.2020.3026384.

Shen, X., Walker, J.P., Ye, N., Wu, X., Brakhasi, F., Boopathi, N., Zhu, L., Yeo, I.Y., Kim, E., Kerr, Y., Jackson, T., 2022. Evaluation of the tau-omega model over bare and wheat-covered flat and periodic soil surfaces at P- and L-band. Remote Sens. Environ. 273. https://doi.org/10.1016/j.rse.2022.112960.

Shen, X., Walker, J.P., Ye, N., Wu, X., Brakhasi, F., Zhu, L., Kim, E., Kerr, Y., Jackson, T., 2023. Evaluation of the tau-omega model over a dense corn canopy at P- and L-band. IEEE Geosci. Remote Sens. Lett. 20, 1–5. https://doi.org/10.1109/LGRS.2023.3315869em ce.

Shi, J., Li, Y., 2013. Development of microwave vegetation index from multi-sensor observations. Int. Geosci. Remote Sens. Symp. 3825–3828. https://doi.org/10.1109/IGARSS.2013.6723665.

Shi, J., Jackson, T., Tao, J., Du, J., Bindlish, R., Lu, L., Chen, K.S., 2008. Microwave vegetation indices for short vegetation covers from satellite passive microwave sensor AMSR-E. Remote Sens. Environ. 112, 4285–4300. https://doi.org/10.1016/J.RSE.2008.07.015.

Vanin, F., Laberinti, P., Donlon, C., Fiorelli, B., Barat, I., Sole, M.P., Palladino, M., Eggers, P., Rudolph, T., Galeazzi, C., 2020. Copernicus imaging microwave radiometer (CIMR): system aspects and technological challenges. Int. Geosci. Remote Sens. Symp. 6535–6538. https://doi.org/10.1109/IGARSS39084.2020.9324259.

Wagner, W., Blöschl, G., Pampaloni, P., Calvet, J.C., Bizzarri, B., Wigneron, J.P., Kerr, Y., 2007. Operational readiness of microwave remote sensing of soil moisture for hydrologic applications. Nord. Hydrol. 38, 1–20. https://doi.org/10.2166/nh.2007.029.

Waldteufel, P., Boutin, J., Kerr, Y., 2003. Selecting an optimal configuration for the soil moisture and ocean salinity mission. Radio Sci. 38. https://doi.org/10.1029/2002rs002744.

Wigneron, J.P., Laguerre, L., Kerr, Y.H., 2001. A simple parameterization of the L-band microwave emission from rough agricultural soils. IEEE Trans. Geosci. Remote Sens. 39, 1697–1707. https://doi.org/10.1109/36.942548.

Wigneron, J.P., Jackson, T.J., O'Neill, P., De Lannoy, G., de Rosnay, P., Walker, J.P., Ferrazzoli, P., Mironov, V., Bircher, S., Grant, J.P., Kurum, M., Schwank, M., Munoz-Sabater, J., Das, N., Royer, A., Al-Yaari, A., Al Bitar, A., Fernandez-Moran, R., Lawrence, H., Mialon, A., Parrens, M., Richaume, P., Delwart, S., Kerr, Y., 2017. Modelling the passive microwave signature from land surfaces: a review of recent results and application to the L-band SMOS & SMAP soil moisture retrieval algorithms. Remote Sens. Environ. 192, 238–262. https://doi.org/10.1016/J.RSE.2017.01.024.

World Bank Group, 2021. Water in Agriculture: Towards Sustainable Agriculture.

World Meteorological Organization, 2022. The 2022 GCOS ECVs Requirements (GCOS-245).

Yao, P., Shi, J., Zhao, T., Cosh, M.H., Bindlish, R., Lu, H., 2019. An L-band brightness temperature disaggregation method using S-band radiometer data for the water cycle observation Mission (WCOM). IEEE J. Sel. Top. Appl. Earth Obs. Remote Sens. 12, 3184–3193. https://doi.org/10.1109/JSTARS.2019.2922780.

Ye, N., Walker, J.P., Rüdiger, C., 2015. A cumulative distribution function method for normalizing variable-angle microwave observations. IEEE Trans. Geosci. Remote Sens. 53, 3906–3916. https://doi.org/10.1109/TGRS.2014.2387574.

Ye, N., Walker, J.P., Bindlish, R., Chaubell, J., Das, N.N., Gevaert, A.I., Jackson, T.J., Rüdiger, C., 2019. Evaluation of SMAP downscaled brightness temperature using SMAPEx-4/5 airborne observations. Remote Sens. Environ. 221, 363–372. https://doi.org/10.1016/J.RSE.2018.11.033.

Ye, N., Walker, J.P., Wu, X., De Jeu, R., Gao, Y., Jackson, T.J., Jonard, F., Kim, E., Merlin, O., Pauwels, V.R.N., Renzullo, L.J., Rudiger, C., Sabaghy, S., Von Hebel, C., Yueh, S.H., Zhu, L., 2021. The soil moisture active passive experiments: validation of the SMAP products in Australia. IEEE Trans. Geosci. Remote Sens. 59, 2922–2939. https://doi.org/10.1109/TGRS.2020.3007371.

Zhang, M.S., Alnasser, F., Entekhabi, D., 2023. L-Band disaggregation with C-Band demonstration using SMAP and AMSR2 data for application to forthcoming CIMR measurements. In: Int. Geosci. Remote Sens. Symp. 2023-July, pp. 1108–1111. https://doi.org/10.1109/IGARSS52108.2023.10281678.